ACS APPLIED MATERIALS & INTERFACES

Research Article

www.acsami.org

Local Control over Nucleation of Epitaxial Thin Films by Seed Layers of Inorganic Nanosheets

Maarten Nijland, Suresh Kumar, Roy Lubbers, Dave H. A. Blank, Guus Rijnders, Gertjan Koster, and Johan E. ten Elshof*

MESA+ Institute for Nanotechnology, University of Twente, P.O. Box 217, 7500 AE Enschede, The Netherlands

Supporting Information

ABSTRACT: Nanosheets of $Ti_{0.87}O_2$ and $Ca_2Nb_3O_{10}$ were synthesized and transferred onto Si substrates by Langmuir−Blodgett deposition. Using pulsed laser deposition, $SrRuO_3$ films were formed on top of these samples. The underlying nanosheets determined both the morphology and crystallographic orientation of the films. $SrRuO_3$ grew preferentially in the $[110]_{pc}$ direction on $Ti_{0.87}O_2$ nanosheets, while growth proceeded in the $[001]_{pc}$ direction on $Ca_2Nb_3O_{10}$ nanosheets (pc refers to the pseudocubic unit cell of $SrRuO_3$). Besides macroscopic control over the out-of-plane crystal direction, single crystal orientations were measured by electron backscatter diffraction on the level of individual nanosheets, indicating that epitaxial growth was achieved on the nanosheets as imposed by their well-defined crystal lattices. The nanosheets also had a clear effect on the magnetic properties of the films, which showed anisotropic behavior only when a seed layer was used. A monolayer consisting of a mixture of both types of nanosheets was made to locally control the nucleation of $SrRuO_3$. In this context, $SrRuO_3$ was used as model material, as it was used to illustrate that nanosheets can be a unique tool to control the orientation of films on a (sub-) micrometer length scale. This concept may pave the way to the deposition of various other functional materials and the fabrication of devices where the properties are controlled locally by the different crystallographic orientations.

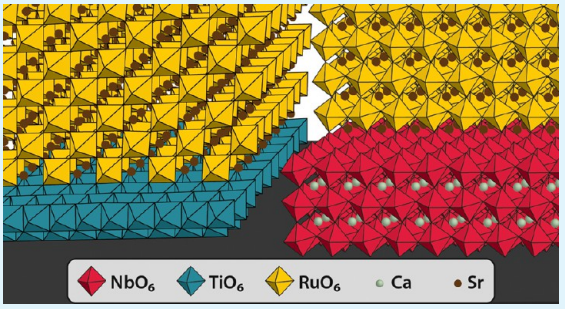

KEYWORDS: *inorganic nanosheets, pulsed laser deposition, anisotropy, mixed orientation, controlled nucleation, ferromagnetic perovskite, $SrRuO_3$*

INTRODUCTION

In thin film laboratories, the structure-property relations of various materials are studied. One particular approach to control the properties of a thin film is by changing its crystallographic orientation. For example, Tebano et al. showed that for films with thicknesses in the range from 3 to 12 nm, $La_{0.67}Sr_{0.33}MnO_3$ was insulating on (001) oriented $LaAlO_3$ but behaved as a metal on (110) oriented $LaAlO_3$.[1] Also, the magnetization characteristics of several manganites were reported to vary with the orientation of the substrate.[2−4] In the field of ferroelectrics, the ferroelectric activity of a material can be tuned by changing its orientation.[5−8] For instance, the ferroelectric response of epitaxial films of Nd-doped $Bi_4Ti_3O_{12}$ could be tuned down to the point were ferroelectricity was completely suppressed by using differently oriented $SrTiO_3$ substrates.[8] A third example of a field where the structure and properties of films were found to vary markedly with the orientation of the substrate is that of nanocomposites made by pulsed laser deposition (PLD). These nanocomposite films are generally formed by self-assembly processes that take place during the simultaneous deposition of two immiscible phases.[9−12]

The previous examples show that the crystallographic orientation is an important parameter that determines the properties of a film. The reason can be found in geometric constraints defined by the unit cell[5−8] but may also be different. For instance, strain imposed by the substrate,[1−4] or anisotropies in the interfacial, surface, or elastic energies, may play a crucial role.[9−12] In all of the examples, the orientations of the films were completely determined by the lattices of the single crystalline substrates. A versatile method to control the orientation of a film on a smaller scale than the typical dimensions of a substrate has so far not been proposed. If such control would be possible, functional films could be designed where certain position dependent properties are determined by the orientations of the crystallites. Thus, an extra degree of freedom would become available for the fabrication of materials with advanced local functionalities.

In this paper, we propose that different types of nanosheets can be used to locally control the nucleation of a film. The concept to use nanosheets for epitaxial growth was first introduced by Kikuta and co-workers in 2007.[13] They showed that the texture of $LaNiO_3$ and $Pb(Zr_{0.3}Ti_{0.7})O_3$ on glass plates could be controlled by the introduction of a seed layer of $Ca_2Nb_3O_{10}$ nanosheets. The films, which were made by chemical solution deposition, showed improved ferroelectric

Received: November 23, 2013
Accepted: January 27, 2014
Published: January 27, 2014

 © 2014 American Chemical Society dx.doi.org/10.1021/am4052624 | ACS Appl. Mater. Interfaces 2014, 6, 2777−2785

properties compared to films made without the nanosheet layer. Later, Shibata et al. used sol−gel processes to deposit textured films of $SrTiO_3$, TiO_2, and ZnO on glass substrates containing monolayers of $Ca_2Nb_3O_{10}$ or MnO_2 nanosheets.[14] Also, PLD was used to form films with certain orientations, even on plastic substrates.[15−17]

In these previous studies, crystalline nanosheets were deposited on amorphous substrates in order to imitate costly single crystal substrates. The, in general, unsurpassed quality of films on single crystal substrates could not be mimicked, though, since the films were in-plane randomly oriented. In this work, we show that nanosheets can be a unique tool to control the nucleation of films on a level that can not be attained on single crystal substrates. In brief, the influence of $Ca_2Nb_3O_{10}$ and $Ti_{0.87}O_2$ nanosheets on the nucleation and properties of $SrRuO_3$ is discussed. $SrRuO_3$ is a conductive perovskite that is ferromagnetic typically below ∼160 K.[18] The model material was selected mainly because strong magnetic anisotropy was expected.[19−23] PLD was used to grow the films on Si substrates, most of which were pre-coated with a single layer of nanosheets. The morphology and crystallographic orientation of these films were controlled by the type of nanosheets that covered the substrates. Epitaxial growth was illustrated and explained by lattice matching with the underlying nanosheets together with continuation of the oxygen octahedral backbones, as illustrated by the graphical abstract. Anisotropic magnetic properties were found when a layer of nanosheets was present but not when $SrRuO_3$ was directly deposited on a Si substrate. The two types of (sub-)micrometer-sized nanosheets were also combined on a single substrate to locally control the orientation of $SrRuO_3$. This experiment illustrates that nanosheets can be used to create films with position dependent properties that are determined by the local crystallographic orientations.

EXPERIMENTAL METHODS

Materials. Anhydrous K_2CO_3 (≥ 99%) was purchased from Fluka; $CaCO_3$ (ACS reagent, chelometric standard), Nb_2O_5 (99.99%, trace metals basis), and MoO_3 (> 99.5%, ACS reagent) were obtained from Sigma-Aldrich; TiO_2 (≥ 99%, technical) and Li_2CO_3 (≥ 99%, purum) were purchased from Riedel-de Haën; nitric acid (65 % *w*/w in water) and tetrabutylammonium hydroxide (40 % *w*/w in water) were provided by Acros Organics and Alfa Aesar, respectively. Ultrapure water with a resistivity of 18.2 MΩ·cm was used, and all chemicals were used as received, without additional purification. Single crystal boron doped (100) silicon wafers (grown by the Czochralski process) were purchased from Okmetic and (001) and (110) oriented $SrTiO_3$ substrates were purchased from CrysTec GmbH. A stoichiometric target of $SrRuO_3$ was obtained from Praxair electronics.

Preparation of the Nanosheets. $Ca_2Nb_3O_{10}$ and $Ti_{0.87}O_2$ nanosheets were prepared similar to the procedures of references 24 and 25. Both types of nanosheets were obtained by solid state calcination followed by cation exchange to achieve exfoliation. $KCa_2Nb_3O_{10}$ was prepared by mixing $K_2CO_3/CaCO_3/Nb_2O_5$ in molar ratios of 1.10/4.00/3.00 and annealing in a capped alumina crucible (100 mL Coors ordered from Sigma-Aldrich) at 1200 °C using the procedure of Table 1. $K_{0.8}[Ti_{1.73}Li_{0.27}]O_4$ was made by intimate grinding of $K_2CO_3/TiO_2/Li_2CO_3/MoO_3$ in molar ratios of 1.00/1.04/0.081/0.76 and calcination in a closed Pt crucible at 1150 °C following the procedure of Table 1. Formation of large crystallites of $K_{0.8}[Ti_{1.73}Li_{0.28}]O_4$ was realized under the conditions mentioned in Table 1 by formation of a liquid flux of K_2MoO_4 that was dissolved in water and filtered out after calcination.

Both layered compounds were stirred in nitric acid to interchange K^+ with H^+ and form $HCa_2Nb_3O_{10}\cdot 1.5H_2O$ and $H_{1.07}Ti_{1.73}O_4\cdot H_2O$. Approximately 20 g of $KCa_2Nb_3O_{10}$ was placed in a 1 L, 5 mol·L^{-1} solution and was stirred with a stirring magnet at 300 rpm for 72 h. Similarly, about 10 g $K_{0.8}[Ti_{1.73}Li_{0.27}]O_4$ was stirred in nitric acid (500 mL, 2 mol·L^{-1}) for 96 h. The latter dispersion was allowed to sediment every 24 h after which the solution was removed by decantation and replaced by a fresh one. After protonation, both powders were filtered by vacuum filtration (Whatman 1450-055) and washed with a copious quantity of water (10 times).

Table 1. Annealing Sequences Used in a Chamber Furnace (Carbolite) for Solid State Synthesis of the Parent Compounds (A Holdback Temperature of 20 °C Was Used)

powder	ramp rate (°C·min^{-1})	temp. °C	duration (h)
$KCa_2Nb_3O_{10}$	5	800	4
	0.5	1200	10
	5	25	
$K_{0.8}[Ti_{1.73}Li_{0.28}]O_4$	3	1150	0.5
	0.1	950	
	5	25	

To obtain $Ca_2Nb_3O_{10}$ nanosheets, 0.4 g of $HCa_2Nb_3O_{10}\cdot 1.5H_2O$ was suspended in 100 mL water and 480 μL of the 40 % commercial aqueous solution of tetrabutylammonium hydroxide (exfoliation agent) was added. The $Ti_{0.87}O_2$ nanosheets were formed by adding 0.3 g of $H_{1.07}Ti_{1.73}O_4\cdot H_2O$ and 635 μL exfoliation agent to 200 mL water. Both solutions were shaken vigorously for 1 min after preparation and then kept on a rocking shaker. To increase stability, the solution containing $Ca_2Nb_3O_{10}$ nanosheets was diluted 9 times after 14 days of exfoliation and the solution containing $Ti_{0.87}O_2$ nanosheets was diluted 3.3 times after 21 days. Prior to making these stock solutions, the solution containing $Ca_2Nb_3O_{10}$ nanosheets was stirred until all of the precipitate had dispersed in the solution, while the other solution was decanted 30 min after it had been removed from the rocking shaker.

Langmuir−Blodgett Deposition. The silicon wafers with native oxide layer were cut into pieces of about 1 × 1.5 cm^2. The substrates were first cleaned on a hot plate at 250 °C with a jet of supercritical CO_2 and then in an oxygen plasma cleaner (Harrick plasma) at 30 W for 15 min. A KSV minimicro double-barrier Langmuir trough with a vertical lifting configuration was used to deposit the nanosheets on the substrates.

Three types of monolayers were deposited on the substrates, that is, $Ti_{0.87}O_2$, $Ca_2Nb_3O_{10}$ and a mixture of both types of nanosheets. For the samples with a dense packing and in the case of $Ti_{0.87}O_2$ nanosheets, depositions were performed at a surface pressure Π = 20 mN·m^{-1}. A 12.3 times dilution of the stock solution was used for these depositions. Without further diluting the stock solution of $Ca_2Nb_3O_{10}$ nanosheets and by using Π = 14 mN·m^{-1}, a high coverage of nanosheets was obtained. In the case when a mixture of both types of nanosheets was desired, 10 mL of each stock solutions was mixed with 30 ml water. The resulting solution was added to the Langmuir trough 15 min after its preparation and a deposition was performed at Π = 17.5 mN·m^{-1}. The isotherms showing the surface pressure versus compression and atomic force microscopy images of the resulting monolayers can be found in the Supporting Information.

Pulsed Laser Deposition of Strontium Ruthenate. $SrRuO_3$ films were deposited by pulsed laser deposition using the conditions of Kuiper et al.[26] All depositions were performed in a 1:1 O_2 and Ar environment of 0.30 mbar. The substrate temperature was controlled by a thermocouple inside the heater at 670 °C.

The laser beam was produced by a 248 nm KrF excimer laser (LPXPro from Coherent, Inc.) with a typical pulse duration of 20 to 30 ns. A square mask of 55.9 mm^2 with rounded corners was used to select the most homogeneous part of the laser beam. The laser was then focused on the stoichiometric $SrRuO_3$ target to a spot size of 1.8 mm^2. The voltage was adjusted to yield a laser fluence of 2.1 J·cm^{-2} on the target. The laser repetition rate was set at 1 Hz and the target to substrate distance was kept at 5 cm.

The target was pre-ablated at 5 Hz for 6 min to remove possible surface contaminations. All depositions were carried out for 60 min,

yielding a layer thickness of 34 ± 7 nm. After deposition, the samples were allowed to cool to room temperature at a maximum rate of 20 °C·min^{-1} in an environment of 100 mbar O_2.

Analysis and Characterization. The topography of the samples was analyzed with a Dimension Icon atomic force microscope (Bruker AXS) using the standard tapping mode option. For selected samples, the relative coverage of nanosheets on the substrates was determined. In these cases, atomic force microscopy scans were made on at least seven different locations on the sample. The data were subsequently processed using Gwyddion 2.29 and the resulting images were analyzed by ImageJ 1.45s to obtain a value for the relative coverage of nanosheets.

Crystallographic information was obtained with a D8 Discover diffractometer (Bruker AXS). Electron backscatter diffraction was performed on a Merlin field emission microscope (Zeiss) equipped with an angle selective backscatter detector. The electron backscatter diffraction data were analyzed by assuming a cubic $SrRuO_3$ crystal structure. In addition, an ultra-high vacuum Orion Plus helium ion microscope (Zeiss) equipped with an Everhardt−Thornley detector (to record images based on secondary electrons) was used.

The samples were cut to sizes of 17 ± 2 mm^2 after which magnetization measurements were conducted on a vibrating sample magnetometer (Physical Properties Measurement System by Quantum Design). The magnetic moments were determined as a function of the magnetic field and temperature, with the magnetic field applied parallel and perpendicular to the surfaces of the samples. The error bars and deviations used in this article all represent a confidence of 95% (two times the standard deviation).

RESULTS AND DISCUSSION

Influence of Nanosheets on the Morphology of Strontium Ruthenate. As can be seen from the tapping mode atomic force microscopy (TM-AFM) images in Figure 1, the topography of $SrRuO_3$ was influenced by the underlying nanosheets. On the parts of the substrates that were not covered by nanosheets, larger and more separated grains were found than on the areas that did contain nanosheets. This observation is corroborated by the values for the root mean square (RMS) roughness. For $SrRuO_3$ on $Ca_2Nb_3O_{10}$ nanosheets, $Ti_{0.87}O_2$ nanosheets, and parts free from nanosheets, the RMS roughnesses were R_q = 5.8 nm, 4.4 nm, and 11 nm, respectively. These values are significantly larger than those measured for $SrRuO_3$ deposited on single crystalline substrates such as (001) $SrTiO_3$ ($SrRuO_3$ deposited on this substrate using the same conditions had an RMS roughness of R_q = 0.24 nm; see Supporting Information). Note that the AFM images of Figure 1 were made on samples with a relative sparse distribution of nanosheets. The reason to show these images is that the different morphologies of $SrRuO_3$ on and off the nanosheets are well visible. Similar film morphologies were obtained on densely packed monolayers of nanosheets (see Supporting Information), which were used for all further analysis and characterization.

Marked differences were observed between the morphologies of the films on $Ca_2Nb_3O_{10}$ and $Ti_{0.87}O_2$ nanosheets. The films on $Ca_2Nb_3O_{10}$ nanosheets (Figure 1a,b) were atomically smooth but contained deep trenches that formed a maze of nanostructures that meandered over the substrate. The trenches preferentially ran into two directions on a single nanosheet. This observation is also illustrated by the inset in Figure 1b, which shows the existence of fourfold symmetry in the two dimensional slope distribution analysis of the AFM image. The symmetry in the slope distribution analysis is a strong indication for epitaxy on the $Ca_2Nb_3O_{10}$ nanosheets, where facets follow preferred crystallographic planes of $SrRuO_3$. On

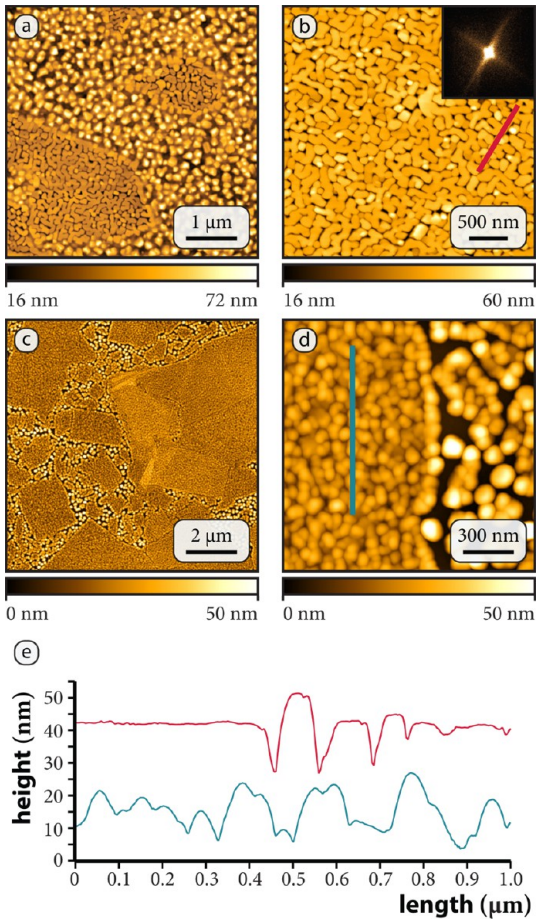

Figure 1. TM-AFM height images of $SrRuO_3$ deposited on Si substrates containing nanosheets. (a, b) $Ca_2Nb_3O_{10}$ nanosheets used as seed layer; (c, d) $Ti_{0.87}O_2$ nanosheets used. The inset in part b shows the slope distribution analysis from the corresponding AFM height image. The height profiles in part e were measured on the lines in parts b (upper red line) and d (lower blue line).

$Ti_{0.87}O_2$ nanosheets the $SrRuO_3$ layer had a typical grain structure in which no such symmetry could be found (Figure 1c,d). Regardless of the type of nanosheets that was used, the morphologies of the films were not significantly influenced by changing the deposition pressure between 0.03 and 0.6 mbar, or the substrate temperature between 600 and 700 °C.

The observed strong variation in morphologies may be explained both by thermodynamic and kinetic considerations. Kinetically, roughness is determined by surface chemistries (e.g., surface charges, contaminations, or dislocations), which may affect sticking coefficients or diffusivities during deposition.[26,27] Thermodynamically, roughness can be caused by stress or by large surface or interfacial energies.[28]

X-ray diffraction and electron backscatter diffraction results discussed below indicated epitaxial growth of $SrRuO_3$ on the individual (single crystalline) nanosheets. Relatively large lattice mismatches between the nanosheets and $SrRuO_3$ and consecutive large elastic strain from registry of the two lattices led to rapid development of stress and may explain roughening of these films. The lattice mismatch for $(001)_{pc}$ oriented growth of $SrRuO_3$ (a_{pc} = 3.928 Å) on $Ca_2Nb_3O_{10}$ nanosheets (a_c = 3.86 Å) is +1.7 %. The mismatch for $(110)_{pc}$ oriented growth of $SrRuO_3$ on $Ti_{0.87}O_2$ nanosheets (a = 3.76 Å, b = 2.97 Å) is +4.3% parallel to the a-axis and −6.9% parallel to the b-axis of

the nanosheets. (labels pc and c refer to a pseudo-cubic and cubic unit cell, respectively). For comparison, the lattice mismatch is +0.6% with $SrTiO_3$. The excessive growth of crystallites that was observed in between the nanosheets may be explained by suppression of nucleation due to absence of a periodic potential in the amorphous oxide layer on Si.

Large interfacial energies may also have caused roughening of the films. In particular, the $(110)_{pc}$ oriented film may have coarsened due to anisotropy in the surface energy. Generally in perovskite oxides, the $(001)_c$ planes have the lowest surface energy.[29−32] The fact that the $(001)_{pc}$ oriented crystallites on $Ca_2Nb_3O_{10}$ nanosheets had atomically smooth surfaces and square-shaped facets, indicates that $SrRuO_3$ forms no exception to this generality. Therefore, the $(110)_{pc}$ oriented film may have preferentially formed $(001)_{pc}$ surface planes, thereby increasing its roughness. This theory is further enforced by the high roughness that was measured on the film deposited on (110) $SrTiO_3$ (R_q = 3.5 nm).

Influence of Nanosheets on the Orientation of Strontium Ruthenate. The X-ray diffraction (XRD) data in Figure 2a shows the result of $\theta-2\theta$ scans on different films. The bottom curve was obtained from a sample where $SrRuO_3$ was deposited directly on a silicon substrate, the middle curve was obtained when a layer of $Ti_{0.87}O_2$ nanosheets with a relative coverage of 96.3 ± 0.9 % was used and the top curve was obtained with a seed layer of $Ca_2Nb_3O_{10}$ nanosheets having a relative coverage of 95.7 ± 1.6%. When $SrRuO_3$ was directly deposited on silicon, no significant peaks other than those from the substrate were found. When $Ti_{0.87}O_2$ nanosheets were used, the strongest peak was found at 2θ = 32.3°. A rocking curve was made at this angle by scanning ω in a window of 18° (Figure 2b). The full width at half maximum (FWHM) of this curve was 3.4°. A different orientation was measured on $Ca_2Nb_3O_{10}$ nanosheets, where peaks were observed at 2θ = 22.7° and 46.3°. In this case an additional peak was observed at 2θ = 44.4°, having an intensity of 4% compared to the peak at 2θ = 46.3°. The rocking curve that was made at 2θ = 46.3° had a FWHM of 1.3° (Figure 2c).

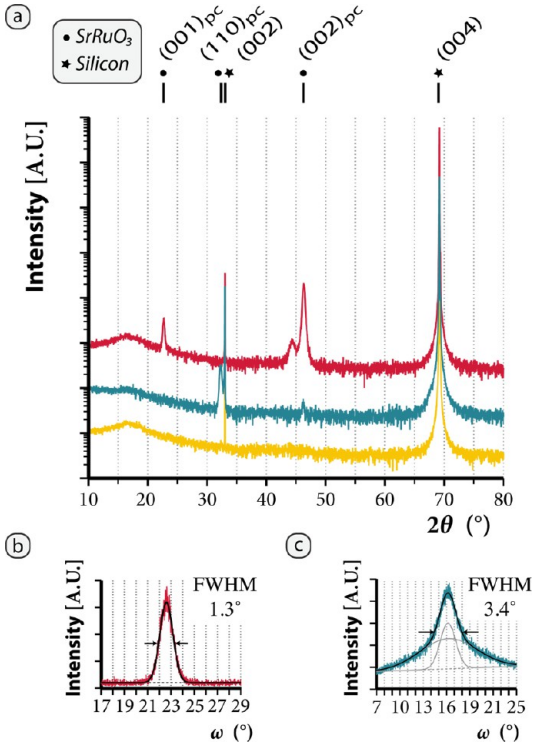

Figure 2. (a) XRD patterns of $SrRuO_3$ deposited on silicon (yellow curve) on silicon containing a monolayer of $Ti_{0.87}O_2$ nanosheets (blue curve, multiplied by a factor of 10) and on silicon containing $Ca_2Nb_3O_{10}$ nanosheets (red curve, × 100). The black lines above the graph indicate the theoretical positions of the diffraction spots of bulk $SrRuO_3$ and Si. The rocking curve in part b was made on the sample containing $Ca_2Nb_3O_{10}$ nanosheets (2θ = 46.28°), the rocking curve in part c was made on the sample containing $Ti_{0.87}O_2$ nanosheets (2θ = 32.26°). The curve in part b was fitted with a single Gaussian function, while two Gaussian functions were used to fit the curve in part c (the background was fitted with a linear function).

Control over crystallographic orientation by nanosheets is illustrated by the fact that film peaks were observed only when $SrRuO_3$ was deposited on nanosheets. The absence of film peaks in the case where $SrRuO_3$ was directly deposited on silicon can be explained by the lack of preferred orientation in this case, together with the absolute amount of material in our films. The peak observed for the film on $Ti_{0.87}O_2$ nanosheets is matching well with the $(110)_{pc}$ orientation of $SrRuO_3$. Also, the $(001)_{pc}$ and $(002)_{pc}$ planes of $SrRuO_3$ diffract at angles where the two main peaks were found for the film on $Ca_2Nb_3O_{10}$ nanosheets.[33] The ω rocking curves further confirmed preferred orientations of the crystallites when deposited on nanosheets. Thus, preferred out-of-plane orientations of the films were confirmed when interlayers of nanosheets were present.

The observed preferential out-of-plane orientation was in both cases expected from the lattice matching with the underlying nanosheets. After all, pseudo-cube on cube epitaxy of $SrRuO_3$ on $Ca_2Nb_3O_{10}$ nanosheets is most likely in the $[001]_{pc}$ direction, while the rectangular structure of the $Ti_{0.87}O_2$ nanosheets will most likely promote growth in the $[110]_{pc}$ direction. Besides, epitaxy is likely in these directions because then the oxygen octahedra of the films and nanosheets are aligned, resulting in a continuous octahedral backbone through the nanosheets and films. The FWHM of the two rocking curves are significantly different, suggesting that the crystallites were more strongly oriented on $Ca_2Nb_3O_{10}$ than on $Ti_{0.87}O_2$ nanosheets. This observation was also in accordance with our expectations, since the lattice mismatch between $Ca_2Nb_3O_{10}$ and $SrRuO_3$ is significantly smaller than the mismatch between $Ti_{0.87}O_2$ and $SrRuO_3$.

The positions of the peaks for both $SrRuO_3$ on $Ca_2Nb_3O_{10}$ and $Ti_{0.87}O_2$ nanosheets indicate that the films were free from strain (d_{001} = 3.91 nm and d_{110} = 2.77 nm). Most probably, elastic relaxation was accommodated by a large number of dislocations and grain boundaries in the films, which is in line with the observed morphologies, as discussed above. Another cause for release of strain may be found in the 'flexible nature' of the nanosheets, which may have resulted in a relaxed film on a strained seed layer.[17] A rational condition for the latter explanation is that the nanosheets should not clamp to the substrate at the high deposition temperatures. Fractions of the film on $Ca_2Nb_3O_{10}$ nanosheets may have been compressively strained, as that would explain the presence of the small peak (d_{002} = 2.04 nm). It is possible that a fraction of $SrRuO_3$ was strained by the unilamellar nanosheets or by thicker crystallites that had not been completely exfoliated into unilamellar sheets.

Magnetic Anisotropy. Temperature dependent magnetization measurements showed anisotropy when either a layer of $Ti_{0.87}O_2$ or $Ca_2Nb_3O_{10}$ nanosheets was used, but not when

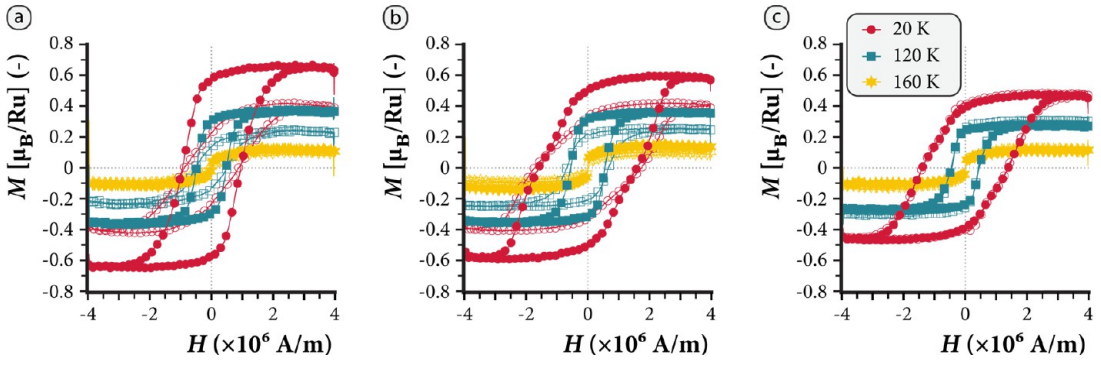

Figure 3. Magnetic hysteresis curves of $SrRuO_3$ films at 20 K, 120 K, and 160 K. The data were obtained from $SrRuO_3$ on (a) $Ca_2Nb_3O_{10}$ nanosheets, (b) $Ti_{0.87}O_2$ nanosheets, and (c) silicon without a layer of nanosheets. The data represented by the closed symbols were obtained by applying the magnetic field parallel to the plane of the surface, while the field was applied out of the plane for the data represented by the open symbols. The curves were obtained after extracting the diamagnetic background signals from the silicon substrates.

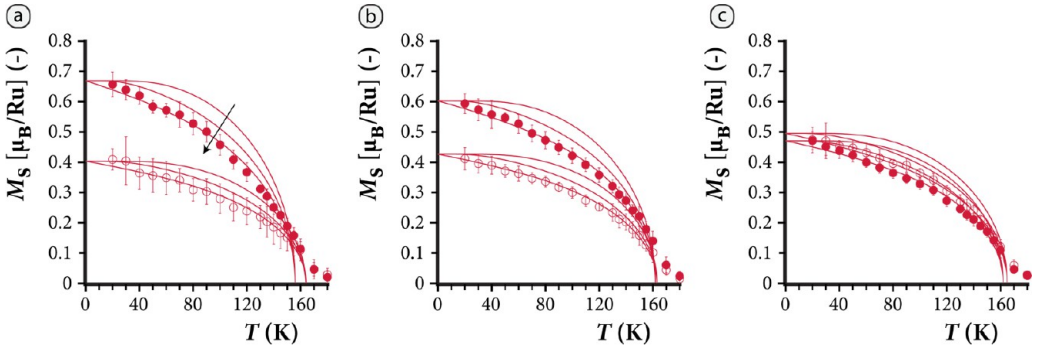

Figure 4. Temperature dependency of the saturation magnetization of $SrRuO_3$ on (a) $Ca_2Nb_3O_{10}$ nanosheets, (b) $Ti_{0.87}O_2$ nanosheets, and (c) silicon without nanosheets. The in-plane measurements (closed circles) and out-of-plane measurements (open circles) were fitted to Brillouin functions calculated from Weiss theory of ferromagnetism. With the assumption of zero external field and for different angular momenta (J), the theoretical curves were fitted (up to 155 K) to the data. Best fits were produced for different values of J by an iterative process, where alternately the absolute saturation magnetization ($I_{S,abs}$) and the Curie point (T_C) were varied. $I_{S,abs}$ and T_C where then chosen from the fit with the lowest least squares. Brillouin curves are shown for J = 1, 4 and ∞, where J increases in the direction of the arrow.

$SrRuO_3$ was directly deposited on Si (Figures 3 and 4). For both films on nanosheets, the easy axis was parallel to the surfaces. Fits of the saturation magnetization versus temperature to theoretical Brillouin functions with J = 1, 4, and ∞ showed that all data were best followed by the Langevin functional dependency (i.e., J = ∞). Ferromagnetic behavior was measured up to ~160 K in all three cases (Figures 4 and 5). The only exception was found when the field was applied in the plane of the surface for the case of $SrRuO_3$ on $Ca_2Nb_3O_{10}$ nanosheets, where the Curie temperature was ~6 K lower.

The anisotropy in the magnetic response for films deposited on nanosheets clearly illustrates that the control over orientation had a significant effect on the properties of the films and was therefore of magnetocrystalline nature. In contrast to these results, the preferred direction of magnetization was measured to be out-of-plane when $SrRuO_3$ was deposited under the same conditions on (110) and (001) oriented $SrTiO_3$ substrates (see Supporting Information). The $SrRuO_3$ films on $SrTiO_3$ were compressively strained while those on nanosheets were free from strain. Due to the strong spin-orbit coupling in $SrRuO_3$, strain has a substantial effect on the magnetization. This was previously observed for $SrRuO_3$ on both (110) and (001) oriented $SrTiO_3$, where the strain was tuned between compressive and tensile by the introduction of a buffer layer.[34,35] In both of these cases, the easy axis rotated into the plane of the surface after changing the strain from

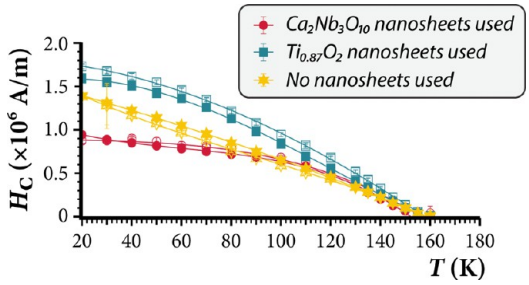

Figure 5. Coercive field as a function of temperature for $SrRuO_3$ deposited on silicon containing $Ca_2Nb_3O_{10}$, $Ti_{0.87}O_2$, and no nanosheets. The data obtained with the field applied in the plane of the surface are represented by closed symbols, while the open symbols represent data obtained with the field applied out-of-plane. The solid lines are fits to a third order function and serve only to guide the eye.

compressive to tensile. Besides by strain, the direction of the easy axis may have been influenced by the roughness. Our films were found to be rougher on the nanosheets than on the $SrTiO_3$ substrates. The preference for out-of-plane magnetization due to the surface anisotropy may have been reduced because of the higher roughness of $SrRuO_3$ on the nanosheets. It is noted that on a macroscopic scale, our $SrRuO_3$ films were randomly oriented in the surface plane, because the nanosheet templates were also randomly oriented. On the other hand, the orientations of the films on the single crystalline substrates were

dx.doi.org/10.1021/am4052624 | ACS Appl. Mater. Interfaces 2014, 6, 2777−2785

fixed in all directions. The two classes of films were therefore essentially different and only for this reason differences in the magnetization behavior are expected.

The measured Curie temperatures are close to the value measured for bulk $SrRuO_3$ ($T_C \approx 165$ K).[18] When $SrRuO_3$ is strained, for example, by clamping on a substrate, the Curie temperature decreases. For example, Gan et al. found a Curie temperature of 150 K for $SrRuO_3$ on a (001) oriented $SrTiO_3$ substrate and showed that this temperature could be increased by 10 K after decoupling the film from the substrate.[36] With respect to this study, the comparatively high Curie temperatures found in this work form yet another indication of relaxation of our films. The deviant value for the Curie temperature of $SrRuO_3$ on $Ca_2Nb_3O_{10}$ nanosheets may be explained by assuming that this film was partly strained, which is in line with the side peak observed in the XRD spectrum of Figure 2.

Signatures of high concentrations of defects were seen from the magnetization measurements, for instance by the high coercivity as plotted in Figure 5 and the large switching areas in the hysteresis curves of Figure 3. These observations can be explained by a large number of free poles, which add up to the magnetostatic energy of the system. Free poles are formed both at the grain boundaries and at imperfections (e.g. dislocations) inside the grains, the latter ones cause pinning of the domains during domain wall motion resulting in an increase of the coercive force (compared to films with less imperfections). We note that the magnetic characterization is in accordance with the AFM and XRD analyses, as all results indicate an abundance of grain boundaries and imperfections in the films. The coercive field was significantly lower when $SrRuO_3$ was deposited on $Ca_2Nb_3O_{10}$ than when it was deposited on $Ti_{0.87}O_2$ nanosheets. This observation is also in agreement with the XRD data, which indicated that crystal growth was controlled to a higher extent by $Ca_2Nb_3O_{10}$ than by $Ti_{0.87}O_2$ nanosheets.

The large concentration of defects and high roughness may explain the observed classical magnetic behavior by the Langevin functional dependency. Furthermore, the absence of a preferred in-plane orientation may have caused the total of all magnetic spins in our films to show classical rather than quantum mechanical behavior. Note that a vibrating sample magnetometer (VSM) is sensitive only for the complete magnetization of a sample. Therefore, no conclusions can be drawn on the magnetic behavior of $SrRuO_3$ on individual nanosheets.

Control over the Crystallographic Orientation on a Single Substrate. One of the great promises of nanosheets is that different kinds can be deposited on a single substrate to locally control the orientation of a film deposited thereon. To illustrate this concept, a mixture containing both $Ca_2Nb_3O_{10}$ and $Ti_{0.87}O_2$ nanosheets was made and transferred onto a single substrate. On top of this monolayer, $SrRuO_3$ was deposited.

After the deposition of nanosheets, a densely packed monolayer with a relative coverage of 95.7 ± 2.0 % was obtained (Figure 6). The two types of nanosheets could be distinguished in the AFM height images by their respective heights ($Ti_{0.87}O_2$ nanosheets have a thickness of 0.75 nm, while $Ca_2Nb_3O_{10}$ nanosheets are 1.44 nm thick[37]). From the contrast in height, the relative coverage of $Ti_{0.87}O_2$ nanosheets was determined to be 69.6 ± 2.3% and the relative coverage of $Ca_2Nb_3O_{10}$ to be 26.1 ± 2.8%. After PLD, both AFM (Figure 6b) and helium ion microscopy images (Figure 7) showed two clearly distinct surface morphologies on the $SrRuO_3$ film. Both

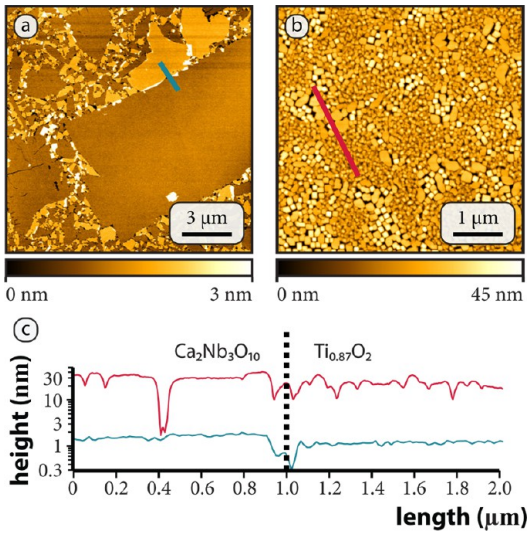

Figure 6. TM-AFM height images of a monolayer of mixed $Ca_2Nb_3O_{10}$ and $Ti_{0.87}O_2$ nanosheets on silicon (a) before and (b) after deposition of $SrRuO_3$. The height profiles of the lines drawn in parts a and b are shown in part c.

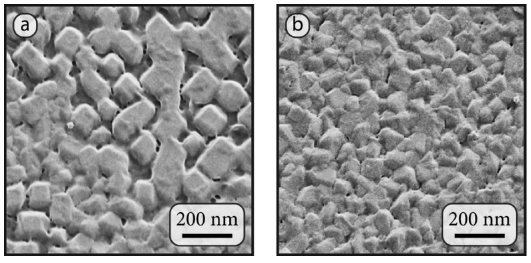

Figure 7. Helium ion microscopy images of $SrRuO_3$ on mixed $Ca_2Nb_3O_{10}$ and $Ti_{0.87}O_2$ nanosheets on silicon. Two different regions are shown that are characteristic for $SrRuO_3$ on (a) $Ca_2Nb_3O_{10}$ and (b) $Ti_{0.87}O_2$ nanosheets (acceleration voltage was 35 kV, working distance was 5.5 mm and sample tilt was 20°).

a smooth layer containing trenches (typical for films on $Ca_2Nb_3O_{10}$ nanosheets) and more regular grains (typically observed on $Ti_{0.87}O_2$ nanosheets) were observed.

In the XRD spectrum (Figure 8), both peaks corresponding to the $(00l)_{pc}$ and $(hh0)_{pc}$ planes were found. The FWHM of the two peaks were a bit larger than those found when $SrRuO_3$ was deposited on a substrate with just one of the two

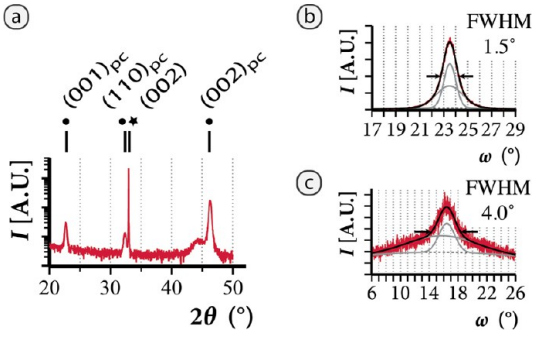

Figure 8. (a) XRD patterns of $SrRuO_3$ on silicon containing both $Ca_2Nb_3O_{10}$ and $Ti_{0.87}O_2$ nanosheets. Rocking curves b and c were obtained with 2θ fixed at respectively 46.30° and 32.36°. Both rocking curves were fitted with two Gaussian functions.

nanosheets. However, also in this case the rocking curve on the $(110)_{pc}$ planes was significantly broader than that on the $(002)_{pc}$ planes. Assuming that the shapes of the two rocking curves were independent of the rocking direction, the volumes (V) under the two curves were estimated by eq 1. This equation was obtained after taking a volume integral over the Gaussian function (I_0 is the intensity at the center of the curve). In a powder diffractogram, the relative intensities of the $(002)_{pc}$ and $(110)_{pc}$ peaks are 35 % and 100 %, respectively.[33] After correcting for these values, the relative amounts of $SrRuO_3$ in the two particular orientations were estimated to be respectively 83% and 17%. This result is another indication that the crystallographic orientation was significantly less well controlled on the $Ti_{0.87}O_2$ nanosheets than on the $Ca_2Nb_3O_{10}$ nanosheets.

$$V = \frac{\pi I_0 \mathrm{FWHM}^2}{4 \cdot \ln 2} \quad (1)$$

Part of the sample was mapped by electron backscatter diffraction (EBSD), the results of which are shown in Figure 9.

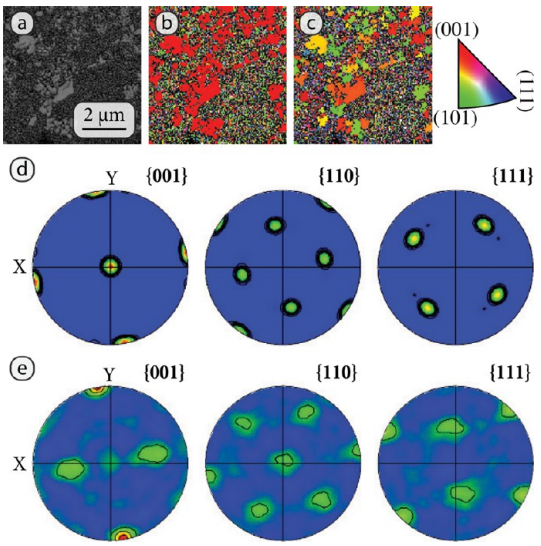

Figure 9. Electron backscatter diffraction images showing the (a) band contrast, (b) inverse pole figure map of the z-direction normal to the surface, (c) inverse pole figure map of the x-direction parallel to the surface, and (d,e) pole figures constructed from two selected areas.

Areas with a clear $(001)_{pc}$ orientation were present, as can be seen from the inverse pole figure map of the direction perpendicular to the surface (z). More interestingly, the inverse pole figure map of a parallel (x) direction showed that the individual $(001)_{pc}$ oriented areas had a single orientation parallel to the plane of the surface. On the areas where no strong $(001)_{pc}$ orientation was observed, the grains were mostly oriented with the $(110)_{pc}$ planes parallel to the surface. The preference, however, was less clear in these areas than in the areas which showed a $(001)_{pc}$ orientation. Two different areas were selected for which a single underlying nanosheet was expected (the areas are highlighted in the Supporting Information). The two pole figures in Figure 9d and e were constructed from the resolved diffraction patterns obtained from these areas. A preferred $(001)_{pc}$ orientation is observed in Figure 9d, while Figure 9e mainly shows $(110)_{pc}$ oriented $SrRuO_3$.

The inverse pole figure maps and pole figures demonstrate that the orientation of the crystallites was controlled both parallel and perpendicular to the direction of growth. Particularly, the two pole figures clearly show that both $(001)_{pc}$ and $(110)_{pc}$ oriented $SrRuO_3$ had a single preferential orientation in all directions. This observation forms a strong indication for epitaxy, where the crystallographic orientations in the film were determined by the underlying nanosheets. The preference was clearer for the $(001)_{pc}$ oriented part than for the $(110)_{pc}$ oriented part. The difference is partly explained by the higher roughness of the film in the $(110)_{pc}$ oriented areas, which led to a smaller band contrast in the diffraction patterns (Figure 9a). Besides, stronger deviations from the $(110)_{pc}$ orientation were also indicated by the XRD patterns. Nevertheless, the single crystal orientations that were most clearly demonstrated by the two pole figures indicate that $SrRuO_3$ grew epitaxially on both $Ca_2Nb_3O_{10}$ and $Ti_{0.87}O_2$ nanosheets.

The magnetic characterization of the film on the mixed nanosheets is shown in Figure 10. We expect the magnetization

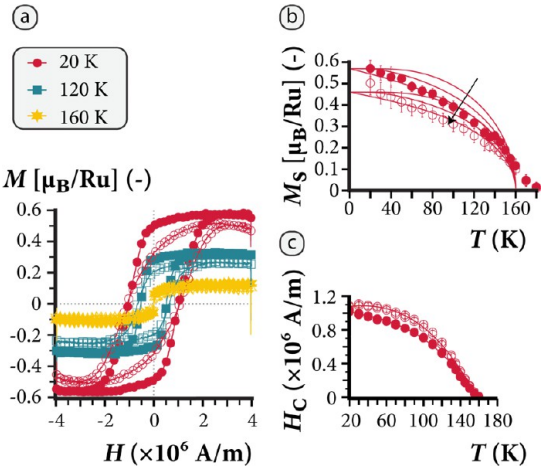

Figure 10. Magnetic characterization of $SrRuO_3$ on silicon containing both $Ca_2Nb_3O_{10}$ and $Ti_{0.87}O_2$ nanosheets. Magnetic hysteresis loops are shown for 20, 120, and 160 K in image (a). Image (b) shows the saturation magnetization versus temperature, together with fits to Brillouin functions (J increases in the direction of the arrow from 1 to 4 to ∞). The coercive field is plotted versus temperature in image (c), where the third order fits serve to guide the eye. Open symbols represent measurements in which the magnetic field was applied perpendicular to the surface of the sample, while closed symbols are used for the data that was obtained with the magnetic field applied parallel to the surface.

properties of this sample to be the convolution of $SrRuO_3$ on $Ca_2Nb_3O_{10}$ and $Ti_{0.87}O_2$ nanosheets. Markedly, the preference for the magnetization parallel to the surface plane was less pronounced than when only one of the two types of nanosheets was used. This difference was probably caused by small experimental variations during the fabrication and measurements of the samples.

Since only data about the complete magnetization of a sample can be obtained with a VSM, local variations within samples could not be mapped. Since the orientation of $SrRuO_3$ is controlled locally by the different nanosheets, we postulate that the film had position dependent magnetic properties that were determined by the type of nanosheet under the film. The relative distribution of the two kinds of nanosheets was

completely random in this case, and we are currently working on methods to control the positioning of nanosheets on a substrate. Such control may pave the way to advanced functional films where the properties are controlled locally by the crystallographic orientation.

CONCLUSIONS

Inorganic nanosheets of $Ca_2Nb_3O_{10}$ and $Ti_{0.87}O_2$ were placed on silicon substrates and used to control the nucleation of $SrRuO_3$ during growth by PLD. The nanosheets proved to influence both the crystallographic orientation and magnetic properties of the films. Magnetic anisotropy was measured when $SrRuO_3$ was deposited on one of the two nanosheets but not when it was deposited directly on a silicon substrate. The typical dimensions of nanosheets allow to control the orientations of films on much smaller length scales than what is typically achieved on single crystalline substrates. This concept was explored by formation of $SrRuO_3$ films on a mixed monolayer comprising both types of nanosheets. Compared to single crystalline substrates, nanosheets are still considered inferior because of poor control over their dimensions, shape, positioning, and orientations. However, nanosheets may offer unique advantages over costly single crystalline substrates. For example, previous work proves that nanosheets can be placed on all sorts of (amorphous) substrates to gain control over the crystallinity of films deposited thereon. With this article, we aim to show that another advantage is the local control over the nucleation of material, which allows tailoring the properties of a material on a (sub-)micrometer scale. Possibly, such control will be having important implications in various fields and will prove useful for applications in data storage and micro-electromechanical systems (MEMS).

ASSOCIATED CONTENT

Supporting Information

Surface pressure versus compression isotherms and AFM images of densely packed $Ca_2Nb_3O_{10}$ and $Ti_{0.87}O_2$ nanosheets before and after deposition of $SrRuO_3$. Analysis and magnetic characterization of $SrRuO_3$ on (001) and (110) oriented $SrTiO_3$. EBSD band contrast image showing the two areas from which pole figures were constructed. This material is available free of charge via the Internet at http://pubs.acs.org/.

AUTHOR INFORMATION

Corresponding Author

*E-mail: j.e.tenelshof@utwente.nl.

Notes

The authors declare no competing financial interest.

ACKNOWLEDGMENTS

We would like to thank E. Houwman and D. Samal for fruitful discussions. We would also like to thank M. Smithers and G. Hlawacek for the scanning electron microscopy and helium ion microscopy measurements, respectively. Financial support from the Chemical Sciences division of the Netherlands Organization for Scientific Research (NWO−CW) in the framework of the TOP and ECHO programmes is gratefully acknowledged.

REFERENCES

(1) Tebano, A.; Orsini, A.; Di Castro, D.; Medaglia, P. G.; Balestrino, G. *Appl. Phys. Lett.* **2010**, *96*, 092505−1−3.
(2) Infante, I. C.; Sanchez, F.; Fontcuberta, J.; Wojcik, M.; Jedryka, E.; Estrade, S.; Peiro, F.; Arbiol, J.; Laukhin, V.; Espinos, J. P. *Phys. Rev. B: Condens. Matter Mater. Phys.* **2007**, *76*, 224415−1−12.
(3) Minohara, M.; Furukawa, Y.; Yasuhara, R.; Kumigashira, H.; Oshima, M. *Appl. Phys. Lett.* **2009**, *94*, 242106−1−3.
(4) Boschker, H.; Mathews, M.; Houwman, E. P.; Nishikawa, H.; Vailionis, A.; Koster, G.; Rijnders, G.; Blank, D. H. A. *Phys. Rev. B: Condens. Matter Mater. Phys.* **2009**, *79*, 214425−1−6.
(5) Aoki, K.; Fukuda, Y.; Numata, K.; Nishimura, A. *Jpn. J. Appl. Phys., Part 1* **1994**, *33*, 5155−5158.
(6) Du, X.; Zheng, J.; Belegundu, U.; Uchino, K. *Appl. Phys. Lett.* **1998**, *72*, 2421−2423.
(7) Lee, H. N.; Hesse, D. *Appl. Phys. Lett.* **2002**, *80*, 1040−1042.
(8) Garg, A.; Barber, Z. H.; Dawber, M.; Scott, J. F.; Snedden, A.; Lightfoot, P. *Appl. Phys. Lett.* **2003**, *83*, 2414−2416.
(9) Zheng, H.; Zhan, Q.; Zavaliche, F.; Sherburne, M.; Straub, F.; Cruz, M. P.; Chen, L. Q.; Dahmen, U.; Ramesh, R. *Nano Lett.* **2006**, *6*, 1401−1407.
(10) Zheng, H.; Straub, F.; Zhan, Q.; Yang, P. L.; Hsieh, W. K.; Zavaliche, F.; Chu, Y. H.; Dahmen, U.; Ramesh, R. *Adv. Mater.* **2006**, *18*, 2747−2752.
(11) Slutsker, J.; Levin, I.; Li, J.; Artemev, A.; Roytburd, A. L. *Phys. Rev. B: Condens. Matter Mater. Phys.* **2006**, *73*, 184127−1−4.
(12) Tan, Z.; Slutsker, J.; Roytburd, A. L. *J. Appl. Phys.* **2009**, *105*, 061615−1−5.
(13) Kikuta, K.; Noda, K.; Okumura, S.; Yamaguchi, T.; Hirano, S. *J. Sol-Gel Sci. Technol.* **2007**, *42*, 381−387.
(14) Shibata, T.; Fukuda, K.; Ebina, Y.; Kogure, T.; Sasaki, T. *Adv. Mater.* **2008**, *20*, 231−235.
(15) Shibata, T.; Ohnishi, T.; Sakaguchi, I.; Osada, M.; Takada, K.; Kogure, T.; Sasaki, T. *J. Phys. Chem. C* **2009**, *113*, 19096−19101.
(16) Tetsuka, H.; Takashima, H.; Ikegami, K.; Nanjo, H.; Ebina, T.; Mizukami, F. *Chem. Mater.* **2009**, *21*, 21−26.
(17) Shibata, T.; Ebina, Y.; Ohnishi, T.; Takada, K.; Kogure, T.; Sasaki, T. *Cryst. Growth Des.* **2010**, *10*, 3787−3793.
(18) Callaghan, A.; Moeller, C. W.; Ward, R. *Inorg. Chem.* **1966**, *5*, 1572−1576.
(19) Kanbayasi, A. *J. Phys. Soc. Jpn.* **1976**, *41*, 1879−1883.
(20) Klein, L.; Dodge, J. S.; Geballe, T. H.; Kapitulnik, A.; Marshall, A. F.; Antognazza, L.; Char, K. *Appl. Phys. Lett.* **1995**, *66*, 2427−2429.
(21) Gan, Q.; Rao, R. A.; Eom, C. B.; Wu, L.; Tsui, F. *J. Appl. Phys.* **1999**, *85*, 5297−5299.
(22) Kim, J. I.; Jung, C. U. *J. Magn.* **2008**, *13*, 57−60.
(23) Palai, R.; Huhtinen, H.; Scott, J. F.; Katiyar, R. S. *Phys. Rev. B: Condens. Matter Mater. Phys.* **2009**, *79*, 104413−1−6.
(24) Ebina, Y.; Sasaki, T.; Watanabe, M. *Solid State Ionics* **2002**, *151*, 177−182.
(25) Tanaka, T.; Ebina, Y.; Takada, K.; Kurashima, K.; Sasaki, T. *Chem. Mater.* **2003**, *15*, 3564−3568.
(26) Kuiper, B.; Blok, J. L.; Zandvliet, H. J. W.; Blank, D. H. A.; Rijnders, G.; Koster, G. *MRS Commun.* **2011**, *1*, 17−21.
(27) Bachelet, R.; Sanchez, F.; Santiso, J.; Munuera, C.; Ocal, C.; Fontcuberta, J. *Chem. Mater.* **2009**, *21*, 2494−2498.
(28) Markov, I. V. *Crystal Growth for Beginners*, 2nd ed.; World Scientific Publishing: Singapore, 2003.
(29) Kim, S. H.; Park, D. Y.; Woo, H. J.; Lee, D. S.; Ha, J.; Seong Hwang, C.; Shim, I. B.; Kingon, A. I. *Thin Solid Films* **2002**, *416*, 264−270.
(30) Sano, T.; Saylor, D. M.; Rohrer, G. S. *J. Am. Ceram. Soc.* **2003**, *86*, 1933−1939.
(31) Alfredsson, M.; Brodholt, J. P.; Dobson, D. P.; Oganov, A. R.; Catlow, C. R. A.; Parker, S. C.; Price, G. D. *Phys. Chem. Miner.* **2005**, *31*, 671−682.
(32) Xu, Z.; Suzuki, M.; Yokoyama, S. *Jpn. J. Appl. Phys.* **2005**, *44*, 8507−8511.
(33) Eysel, W.; Geyer, A. PDF Reference Code: 43−0472. 1992.
(34) Jung, C. U.; Yamada, H.; Kawasaki, M.; Tokura, Y. *Appl. Phys. Lett.* **2004**, *84*, 2590−2592.

(35) Terai, K.; Ohnishi, T.; Lippmaa, M.; Koinuma, H.; Kawasaki, M. *Jpn. J. Appl. Phys.* **2004**, *43*, L227−L229.
(36) Gan, Q.; Rao, R. A.; Eom, C. B.; Garrett, J. L.; Lee, M. *Appl. Phys. Lett.* **1998**, *72*, 978−980.
(37) Osada, M.; Sasaki, T. *J. Mater. Chem.* **2009**, *19*, 2503−2511.